Polymer-Assisted-Water-Alternating-Gas for Improving the CO_2 Flow Properties in Porous Media

Yegane, Mohsen Mirzaie; van Wieren, Thijs; Fadili, Ali; van Batenburg, Diederik; Leblanc, Thierry; Zitha, Pacelli

DOI
10.2118/215024-MS

Publication date
2023

Document Version
Final published version

Published in
Proceedings - SPE Annual Technical Conference and Exhibition 2023

Society of Petroleum Engineers

SPE-215024-MS

Polymer-Assisted-Water-Alternating-Gas for Improving the CO_2 Flow Properties in Porous Media

Mohsen Mirzaie Yegane, Department of Geosciences and Engineering, Delft University of Technology, Delft, The Netherlands / Dutch Polymer Institute (DPI), the Netherlands; Thijs van Wieren, Department of Geosciences and Engineering, Delft University of Technology, Delft, The Netherlands; Ali Fadili and Diederik van Batenburg, Shell Global Solutions International B.V., The Hague, Netherlands; Thierry Leblanc, SNF S.A., ZAC de Milieux, France; Pacelli Zitha, Department of Geosciences and Engineering, Delft University of Technology, Delft, The Netherlands

 DOI 10.2118/215024-MS

This paper was prepared for presentation at the 2023 SPE Annual Technical Conference and Exhibition held in San Antonio, Texas, USA, 16 - 18 October 2023.

Abstract

CO_2 flow in porous media is vital for both enhanced oil recovery and underground carbon storage. For improving CO_2 mobility control and thus improved reservoir sweep efficiency, Water-Alternating-Gas (WAG) injection has often been applied. The effectiveness of WAG diminishes, however, due to the presence of micro-scale reservoir heterogeneity which results in an early breakthrough of gas. We propose Polymer-assisted WAG (PA-WAG) as an alternative method to reduce gas mobility, while also reducing the mobility of the aqueous phase, and consequently improving the performance of WAG. In this method, high molecular weight water-soluble polymers are added to the water slug.

The goal of this work was to investigate the feasibility of PA-WAG and study the transport processes in porous media. An ATBS-based polymer (SAV 10 XV) was chosen as polymer and CO_2 at immiscible conditions as gas. The objective of the experiments was to compare the performance of CO_2, WAG, and PA-WAG injection schemes by conducting a series of X-ray computed tomography (CT)-aided core-flood experiments in Bentheimer cores.

Core-flood results clearly demonstrated the beneficial effects of PA-WAG over WAG and continuous CO_2 injection. Continuous injection of CO_2 led to the recovery factor (RF) of only 39.0 ± 0.5% of the original oil in place (OOIP). In-situ visualization of CO_2 displacement showed strong gravity segregation and viscous fingering because of the contrast in the viscosities and densities of CO_2 and oil. The injection of WAG almost doubled the oil recovery (i.e., RF=76.0 ± 0.5%); however, the water and gas breakthroughs still occurred in the early stage of the injection (0.22 PV for water and 0.27 PV for CO_2). The addition of the polymer to the aqueous phase delayed both the water and CO_2 breakthrough (0.51 PV for water and 0.35 PV for CO_2). This resulted in an additional 10% in the recovery factor. Using a single injection method, polymer adsorption was found to be 79.0 ± 0.5 μg polymer/g rock. The polymer adsorption can reduce the micro-scale permeability and as a result, mitigates the gas channeling. This in turn leads to the delay in CO_2 breakthrough during PA-WAG injection as was evident from in-situ visualization.

This experimental study demonstrated a positive response of PA-WAG compared to WAG and paves the way for its implementation in field applications.

Introduction

CO_2 flow in porous media is vital for carbon utilization and underground storage, both of which contribute to the reduction of the atmospheric concentration of CO_2. Underground storage involves the injection of CO_2 from large stationary sources into deep geological formations [1]. In deep saline aquifers, for instance, the CO_2 is in the supercritical phase and has a liquid-like density between 250–800 kg/m^3 [2]. However, even at this condition, CO_2 density is still substantially lower than the brine density, which exists in deep saline aquifers and may be more than 1200 kg/m^3. As a result, the injected CO_2 will have a strong buoyant drive upward and will not propagate into the lower part of the reservoir.

For enhanced oil recovery (EOR) applications, in which the CO2 is in the gas phase, this effect is much more adverse, as there is a significant contrast between the density of gas-CO_2 and that of oil and brine. This leads to strong gravity override and little oil recovery at the lower parts of the reservoir [3]. Moreover, the viscosity of both supercritical and gas CO_2 at reservoir conditions ranges between 0.05–0.1 cP which is quite smaller than typical values for oil and brine viscosities [4]. This results in viscous fingering and early breakthrough of the CO_2 [5]. Another reason for this early breakthrough is the presence of micro-scale reservoir heterogeneities that can cause CO_2 to channel through the more permeable parts of the reservoir and breakthrough more quickly [6,7]. Combining all these factors can lead to low oil recovery and high gas utilization.

Water-Alternating-Gas (WAG) has been successfully applied to improve the sweep efficiency of the CO_2 injection [8]. The main mechanism during WAG injection is using water to reduce CO_2 mobility and stabilize the front [9]. WAG combines the improved sweep efficiency of water flooding and the displacement efficiency of gas flooding [10]. The effectiveness of WAG diminishes, however, in highly heterogenous, fractured, and thick reservoirs, and long inter-well distances [11], and therefore, requires further improvement for the water and CO_2 slugs. In Brage, an offshore oil field in the North Sea, an early breakthrough of gas occurred followed by low sweep efficiency in the subsequent gas cycles [12]. The reason for this behaviour was the presence of a thin and high permeability layer through which gas could channel and had a premature breakthrough.

Choi et al. investigated the application of gel treatment during CO_2–WAG injection in a heterogeneous reservoir to mitigate the low sweep efficiency [13]. They observed a 31% increase in the oil recovery after the gel treatment. They attributed this to better mobility control because of the reduction in permeability. As for the fractured reservoirs, Chakravathy et al. [6] suggested (a) injecting viscous water (due to the presence of water-soluble polymers in water) into the fracture to divert the CO_2 flow from the fractures and (b) applying cross-linked gel for the purpose of conformance control and water control in the matrix.

Recently, Polymer-Assisted-Water-Alternating-Gas (PA-WAG) has received attention as a method to mitigate the early gas breakthrough and gravity segregation during WAG injection [14]. It involves dissolving high molecular weight water-soluble polymers in water and injecting it alternating with gas injection. Zhang et al. [15] experimentally investigated the effect of coupling CO_2 and polymer injection on the recovery of heavy oil. They found that the coupled injection of CO_2 and polymer leads to a higher recovery as compared to recovery obtained from CO_2–WAG and polymer flooding. Moreover, it had much better gas utilization and reduced the gas consumption of CO_2–WAG to one-third. Li et al. [16] simulated the effectiveness of PA-WAG in a sector model of TR59 of the North Burbank Unit (NBU). They noted that the recovery of PA-WAG was 12% higher than that of WAG. Moreover, Tovar et al. [17] conducted a series of core-flood experiments on cores obtained from NBU. They observed that, in homogenous cores, there is almost a 10% increase in the recovery of WAG when PA-WAG is used. However, there was no meaningful

increase in the recovery factor in heterogeneous cores. There are other simulation works [18-20] that have concluded there is an incremental recovery of 6–11.6% when water-soluble polymers are added to the water slug during WAG injection. There seems to be a consensus that the delay in the gas breakthrough and lower gravity override is what causes this incremental recovery.

However, the flow mechanisms in PA-WAG injection in porous media remain poorly understood. In particular, there is no experimental study that demonstrates the in-situ visualization and discusses how PA-WAG can improve the gravity override and early gas breakthrough of WAG. The objective of this study is to demonstrate experimentally the feasibility of PA-WAG by conducting a series of X-ray computed tomography (CT)-aided core-flood experiments. To this end, several core-flood experiments in Bentheimer cores using different injection schemes were conducted: (a) CO_2 and polymer injection, (b) WAG injection, and (c) PA-WAG injection. The aim of CT scanning during the core-flood experiments was to map the phase saturations at different times of injection. We present new insights on the displacement mechanisms which could only be obtained by CT scanning. Using dual-energy CT scanning, we could visualize a reduction in gravity override and delay the CO_2 breakthrough when PA-WAG was used.

Experiments

Chemicals

Table 1 presents the various chemical components that were used in this study along with their physical properties. The oleic phase, n-hexadecane, which is colorless, was colored with a red colorant (Oil Red O) for the purpose of visualization. The oleic phase was doped with the addition of 20 wt% 1-iododecane for enhancing the CT contrast. The composition of the synthetic seawater (SSW) can be found in Table 2. Core-flood experiments were performed at a pressure of 20 bar and a temperature of 40 °C. At these conditions, CO_2 was in the gas phase and at immiscible conditions. An ATBS-based polymer (SAV 10 XV) at a concentration of 0.2 wt% was chosen as the polymer. The densities and viscosities of the SSW, oil, and SAV 10 XV at core-flood experimental conditions are shown in Table 3.

Table 1—Physical properties of the chemicals. The value of viscosity and density are specific to conditions at atmospheric pressure and 20 °C.

	Chemical Formula	Moleculer weight (g/mol)	Density (g/cm^3)	Viscosity (mPa s)	Supplier
n-hexadecane	$CH_3(CH_2)_{14}CH_3$	226.45	0.775 ± 0.001	3.37 ± 0.06	Merck
Oil Red O	$C_{26}H_{24}N_4O$	408.49	-	-	Sigma-Aldrich
1-iododecane	$CH_3(CH_2)_9I$	268.18	1.257 ± 0.001	-	Sigma-Aldrich
Carbon dioxide	CO_2	44.01	$1.839\pm 0.001\times10^{-3}$	$1.46 \pm 0.50\times10^{-2}$	-
SAV 10XV					SNF S.A.

Table 2—The components used to make the synthetic seawater with their concentrations.

Salt type	Concentration (g/l)
NaCl	24.501
KCl	0.673
$MgCl_2{\cdot}6H_2O$	10.150
$CaCl_2{\cdot}2H_2O$	1.449
$SrCl_2{\cdot}6H_2O$	0.015
$Na_2SO_4{\cdot}10H_2O$	8.717

Salt type	Concentration (g/l)
$NaHCO_3$	0.328
TDS	35.2

Table 3—Physical properties of the SSW, oil, and SAV 10 XV at 40 °C, and atmospheric pressure. The reported shear rate of 15 s^{-1} and 60 s^{-1} correspond to the injection flow rate of 0.5 and 2 cm^3/min respectively.

Fluid	Density (g/cm^3)	Viscosity (cP)
Synthetic seawater (SSW)	1.019 ± 0.001	0.75 ± 0.05
0.2 wt% SAV 10XV (15 s^{-1})	1.026 ± 0.001	11.40 ± 0.20
0.2 wt% SAV 10XV (60 s^{-1})		6.30 ± 0.20
n-hexadecane (including < 0.0006 wt% Oil Red O 20 wt% 1-iododecane)	0.830 ± 0.001	2.26 ± 0.02

Core-flood experiments

Core samples. The core-flood experiments were performed using Bentheimer cores. Bentheimer sandstone cores have high permeabilities and are fairly homogeneous mineralogy (>91 wt% quartz) [21]. The porosity of the core samples was measured using CT scanning. To prepare the sandstone for the core floods, cores were first cut and then dried in an oven for up to 48 hours at 60 ± 1 °C. Afterward, the cores were embedded in an epoxy resin to ensure that flow bypassing along the core was prevented. The resin penetrated the core by approximately 1.0 mm. Thereafter, the cores were machined to an effective diameter of 3.8 ± 0.1 cm and a length of 38.0 ± 0.1 cm. The machined samples were placed in an oven for 15 hours at 40 ± 1 °C to dry. The absolute permeability of each core to SSW was then estimated using Darcy's law.

Experimental set-up. Fig. 1 illustrates the experimental setup for the core-flood study. To introduce the aqueous phases into the core, a dual-cylinder pump (Quizix QX-6000) was employed. The core was positioned in a polyether ether ketone (PEEK) core holder with low X-ray attenuation and encased in a heating sleeve to maintain a constant temperature of 40°C. The core, core holder, and heating sleeve were placed in a fixed horizontal position on the CT bench, as vertical scanning led to undesirable artifacts and yielded no meaningful insights. For the desired back-pressure (BP) of 20 ± 1 bar, a back-pressure regulator connected to a nitrogen cylinder (100 ± 1 bar) was utilized. Fraction collector sampling was used to collect effluents at the outlet at various time intervals. CO_2 was injected into the system via a mass flow controller (Bronkhorst, EL-FLOW) sourced from a dedicated CO_2 supply. The pump indirectly introduced both the oleic phase during primary drainage stages and the polymer solution used for secondary or tertiary recovery by means of a transfer vessel. The pressure drop across various sections of the core was measured using four pressure transducers (KEMA03 ATEX 1561) with a range of ± 300 mbar and an accuracy of ± 1 mbar (three transducers for different core sections and one for the entire core length). Pressure and temperature measurements were recorded at 10-second intervals using a data acquisition system (National Instruments).

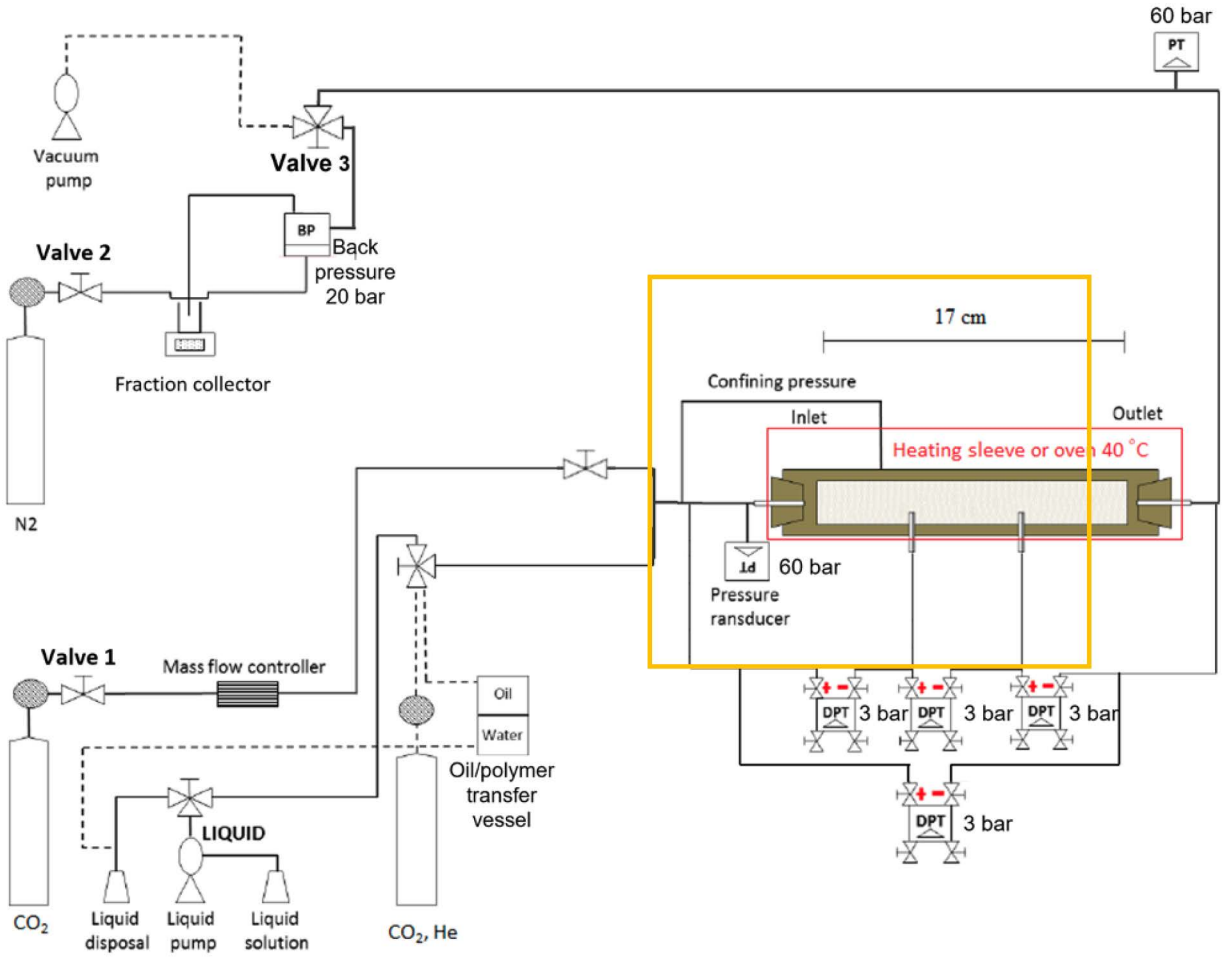

Figure 1—The schematic of the core-flood experimental setup. BP= back pressure, DPT = differential pressure transducer.

Experimental procedure. A total of 4 core-flood experiments were conducted in this study. Table 4 shows an overview of these experiments. As mentioned, all the experiments were carried out at pressure and temperature of 20 ± 1 and 40 ± 1°C respectively. In Table 5, an overview of the procedure for all 4 experiments is presented. After ensuring that there are no leaks, the system is flushed with carbon dioxide (CO_2) at a pressure of 5 ± 0.5 bar for the removal of air in the set-up. Thereafter, the setup is vacuumed to remove any remaining gas. SSW was then injected for 10.00 ± 0.05 pore volumes (PV) at a flow rate of 2.00 ± 0.02 mL/min to saturate the core. During brine saturation, the backpressure is increased to 20 bar to ensure the complete dissolution of CO_2 in the brine. The average permeability of the core used was determined by applying Darcy's law and varying the injection rates of brine.

Table 4—The core-flood experiments performed in this study along with their properties. PF= polymer flooding, CO_2 = CO_2 flooding, WAG= water alternating gas, PA-WAG= polymer-assisted water alternating gas.

Exp.	Core type	Porosity (%)	Permeability (D)	Length (cm)	Diameter (cm)	Oil type
Exp. 1 (PF + CO_2)	Bentheimer	23.1 ± 0.1	1.85 ± 0.07	17.00 ± 0.10	3.80 ± 0.10	*n*-hexadecane
Exp. 2 (CO_2 + PF)	Bentheimer	21.6 ± 0.1	2.69 ± 0.10	17.00 ± 0.10	3.80 ± 0.10	*n*-hexadecane
Exp. 3 (WAG)	Bentheimer	21.6 ± 0.1	2.67 ± 0.10	17.00 ± 0.10	3.80 ± 0.10	*n*-hexadecane
Exp. 4 (PA-WAG)	Bentheimer	21.9 ± 0.1	2.66 ± 0.10	17.00 ± 0.10	3.80 ± 0.10	*n*-hexadecane

Table 5—The procedure of the performed core-flood experiments.

Stage	Description	Back pressure (bar)	Flow rate (cm^3/min)	Injection pressure (bar)	Remarks
1	CO_2 flushing	-	-	5	
2	Vacuuming	-	-	-	
3	Brine saturation	20	2	-	
4	Permeability test	20	1.0, 2.0, 3.0, 4.0, 5.0		To estimate the core absolute permeability
5	Oil injection	20	0.5		For the experiments with oil, Exp. 2, through 10
6	Oil bump flood	20	0.5, 2.5, 5.0	-	To estimate the oil relative permeability
7	Polymer flooding followed by CO_2 flooding	20	Polymer: 0.5 CO_2: 0.5		Exp. 1
	CO_2 flooding followed by Polymer flooding	20	Polymer: 0. 5 CO_2: 0.5		Exp. 2
	WAG injection	20	CO_2: 0.5, water: 2.0	-	Exp. 3
	PA-WAG injection	20	CO_2: 0.5, polymer: 2.0	-	Exp. 4

Primary drainage was initiated by injecting approximately 6 pore volumes (PV) of oil. The flow rates were adjusted during the final PV of oil injection to obtain the oil end-point relative permeability (k^e_{ro}), which corresponded to the point where S_wc (water saturation at irreducible water saturation) was reached. Afterward, depending on the experiment, polymer flooding, CO_2 flooding, WAG, or PA-WAG injection was initiated.

Polymer and CO_2 were injected at S_{oi} for 5 PV each, and constant backpressure of 20 bar. During the WAG and PA-WAG injection processes, a total of six cycles were performed. Each cycle involved injecting a water slug of 0.22 PV followed by a CO_2 slug of 1.30 PV at S_{oi}. CO_2/polymer/WAG/PA-WAG injection continues for each experiment until no more oil was produced. The core-floods were assessed in terms of oil recovery, pressure data, CT images, and saturation profiles.

CT scan. CT scans were conducted at specific intervals during the core-flood experiments using a Siemens SO-MATOM Definition CT scanner equipped with full dual-energy scanning capabilities. These scans aimed to examine phase saturation distributions and analyze three-phase fluid systems. The core was positioned horizontally on the CT scanner bed. Dual X-ray tubes were employed simultaneously, with one operating at 80 kV voltage and 550 mA current, and the other at 140 kV voltage and 250 mA current. Each scan encompassed 302 slices, each measuring 0.6 mm in thickness. Every slice consisted of 512 × 512 pixels, with a pixel size of 0.2 × 0.2 mm. Spiral scanning mode was utilized for scanning the core. Data obtained from the CT scans were analyzed and visualized using ImageJ and Avizo software.

Throughout the entire study, the porosity of the cores was determined by utilizing the single energy 140 kV data (referred to as subscript 1 in CT analysis formulas) and applying the following equation:

$$\phi_1 = \frac{CT_{wet_1} - CT_{dry_1}}{CT_{brine_1} - CT_{air_1}} \quad (1)$$

where ϕ represents the porosity, while CT_{dry_1}, CT_{wet_1}, CT_{brine_1}, and CT_{air_1}, refer to the CT responses in Hounsfield Units (HU) for the dry core, brine saturated core, brine phase in bulk and air phase in bulk at the energy of 140 kV.

Throughout the entire study, the estimation of oil and water saturations in a two-phase system was conducted using single energy 140 kV data, employing the following equations:

$$S_o = \frac{1}{\phi_1}\frac{CT_1 - CT_{wet_1}}{CT_{oil_1} - CT_{brine_1}} \tag{2}$$

$$S_w = 1 - S_0 \tag{3}$$

where S_o, S_w, CT_1, and CT_{oil_1} respectively denote the oil saturation, water saturation, CT response in Hounsfield Units (HU) of the scanned core at the particular time of interest, and the CT response of the oil phase in bulk.

To determine the saturation distribution in a three-phase system, it is necessary to utilize dual-energy CT data. Throughout the entire study, the CT response data at 140 kV (subscript 1) and 80 kV (subscript 2) is employed to estimate the saturations as follows:

$$S_0 = \frac{\left(CT_1 - CT_{wet_1}\right)\left(CTdry_2 - CT_{wet_2}\right) - \left(CT_2 - CT_{wet_2}\right)\left(CTdry_1 - CT_{wet_1}\right)}{\phi_1\left(CT_{oil_1} - CT_{brine_1}\right)\left(CTdry_2 - CT_{wet_2}\right) - \phi_2\left(CT_{oil_2} - CT_{brine_2}\right)\left(CTdry_1 - CT_{wet_1}\right)} \tag{4}$$

$$S_g = \frac{\left(CT_1 - CT_{wet_1}\right)\phi_2\left(CT_{oil_2} - CT_{brine_2}\right) - \left(CT_2 - CT_{wet_2}\right)\phi_1\left(CT_{oil_1} - CT_{brine_1}\right)}{\phi_2\left(CT_{oil_2} - CT_{brine_2}\right)\left(CTdry_1 - CT_{wet_1}\right) - \phi_1\left(CT_{oil_1} - CT_{brine_1}\right)\left(CTdry_2 - CT_{wet_2}\right)} \tag{5}$$

$$S_w = 1 - S_0 - S_g \tag{6}$$

where S_g represents the gas saturation. It should be pointed out that for the analysis of three-phase saturation distribution, the 80 kV single energy porosity is necessary. In these instances, Equation 1 is applied with the use of subscript 2 instead of subscript 1.

Results and discussion

Table 6 presents the key outcomes of the conducted core-flood experiments. The obtained end-point relative permeabilities exhibit notable consistency with the findings reported by Janssen et al. [22] for Bentheimer sandstone, albeit minor variations among individual experiments (i.e., cores) were observed.

Table 6—The main results from the core-flood experiments carried out in this study. BT_w and BT_g denote the breakthrough time of the aqueous and gas phases, respectively. S_{oi}, $k_{e_{ro}}$, and RF represent initial oil saturation, remaining oil saturation, oil end-point relative permeability, and recovery factor

Exp.	BT_w	BT_g	S_{oi}	S_{oR}	$k_{e_{ro}}$	RF (%)
Exp. 1	0.57 ± 0.03	0.51 ± 0.03	0.75 ± 0.03	0.27 ± 0.03	0.58 ± 0.04	63.9 ± 3.1
Exp. 2	0.32 ± 0.03	0.42 ± 0.03	0.70 ± 0.03	0.19 ± 0.03	0.53 ± 0.04	72.4 ± 3.1
Exp. 3	0.22 ± 0.03	0.27 ± 0.03	0.78 ± 0.03	0.19 ± 0.03	0.52 ± 0.04	75.8 ± 3.1
Exp. 4	0.51 ± 0.03	0.35 ± 0.03	0.78 ± 0.03	0.11 ± 0.03	0.54 ± 0.04	85.5 ± 3.1

This section subsequently delves into the following subsections: primary drainage, polymer flooding followed by CO_2 flooding (Exp. 1), CO_2 flooding followed by polymer flooding (Exp. 2), and Water-Alternating-Gas (WAG) injection (Exp. 3) vs. Polymer-Assisted Water-Alternating-Gas (PA-WAG) injection (Exp. 4). In order to evaluate the effectiveness of the different injection strategies, the parameters such as pressure drop, oil recovery as well as CT data are comprehensively analyzed.

Primary drainage

In the primary drainage phase, the core was subjected to the injection of the oil phase at a consistent flow rate of 0.5 cm³/min. This was followed by a bump flooding process conducted at different flow rates ranging from 0.5 to 2.5 cm³/min. The objective was to achieve the connate water saturation (S_{wc}) and subsequently establish the initial oil saturation (S_{oi}). Within this section, we present and analyze the outcomes of a representative primary drainage stage, encompassing the total pressure drop profile, CT images, and the associated saturation profiles.

Pressure drop. Fig. 2 illustrates the total pressure drop profile for the primary drainage stage of the PA-WAG experiment (Exp. 4), which is representable for the core-flood experiments performed in this study. Oil breakthrough occurred at an approximate value of 0.74 ± 0.03 pore volumes (PV). Once the oleic phase reached the core inlet, there was a noticeable abrupt increase in pressure drop attributed to the capillary entry pressure, resulting in a value of approximately 40 ± 3 mbar. Subsequently, the pressure drop steadily rose until it reached its peak value of 78 ± 3 mbar at the time of the oil breakthrough. Following the breakthrough, the pressure drop exhibited fluctuating behavior which can be attributed to the mobilization and production of the remaining water in the core. Overall, there is a decreasing trend in the pressure drop until it stabilized towards a steady-state value corresponding to oil flow at the connate water saturation (S_{wc}), which was determined to be 0.22 ± 0.03. Additionally, the oil end-point relative permeability (k_{ero}) was estimated to be 0.58 ± 0.04.

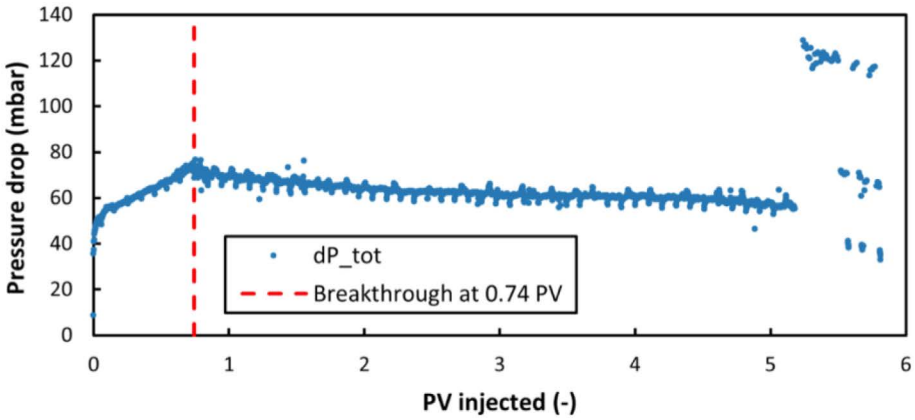

Figure 2—Total pressure drop profile for the primary drainage during Exp. 4. After ~5 PV, the injection flow rate was increased to 2.5 cm³/min to initiate the bump flood for the oil phase and further reduce the water saturation towards S_{wc}.

CT images. Fig. 3 presents the CT images and corresponding oil saturation (S_o) profiles for primary drainage Exp. 4. During the primary drainage phase, the displacement of water (light blue/white) by oil (blue/green) occurred in a piston-like4 manner, as depicted in Fig. 3A. Towards the end of the primary drainage, the relatively low oil saturation observed near the outlet region can be attributed to the capillary end effect. This suggests the buildup of water (wetting phase) near the outlet to satisfy the zero capillary pressure condition at the outlet boundary [23]. The corresponding oil saturation profiles exhibit a sharp shock front region. Ultimately, an averaged initial oil saturation (S_{oi}) of 0.78 ± 0.03 was attained. It is important to note that the final scan conducted during the primary drainage phase was performed at 9.35 ± 0.03 PV of oil injection, which exceeds the PV reported in Fig. 2. This deviation occurred due to complications encountered with the medical CT scanner during the experiment. Initially, oil injection commenced at a very low flow rate for over 3 PV until the medical CT scanner was repaired and the experiment could proceed. Interestingly, the additional pore volumes of oil injected into the core did not impact the oil saturation. It became evident that the initial oil saturation had already been attained after approximately 6 PV of injection.

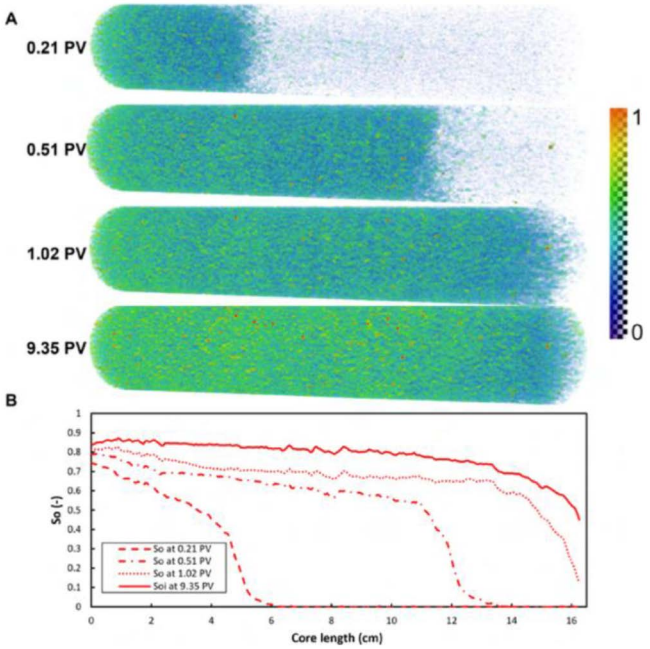

Figure 3—Displacement profile of the oil during primary drainage during PA-WAG in Bentheimer experiment (Exp. 4) with (A) CT images and (B) oil saturation profile.

Polymer flooding followed by CO_2 flooding (Exp. 1)

The conducted experiment involved the recovery of oil from a Bentheimer core utilizing polymer flooding as a secondary mode and CO_2 as a tertiary mode. The findings presented in this section are analyzed based on pressure drop profiles, CT images, and oil recovery data.

Pressure drop. Fig. 4 illustrates the pressure drop profile for Exp. 1. During the injection of the polymer solution into the core at a flow rate of 0.5 cm^3/min, a consistent rise in pressure drop was observed, reaching a value of 1300 ± 10 mbar until the breakthrough of the polymer occurred at approximately 0.57 ± 0.03 PV. The observed pressure drop is significantly higher compared to the primary drainage phase, owing to the considerably greater viscosity of the polymer in comparison to the oil (see Table 3). Furthermore, it is worth noting that the breakthrough of the polymer was observed at a later stage compared to the water breakthrough reported by Janssen et al. [22]. In their study, waterflooding was conducted using a Bentheimer core and n-hexadecane as the oleic phase as well, and the water breakthrough occurred at approximately 0.37 ± 0.02 PV. Shortly after the polymer breakthrough, a slight emulsion became visible in the recovered fluids. This observation may be attributed to the potential interaction between the components present in the SAV 10XV polymer and n-hexadecane used in the experiment. Fluctuations in the pressure drop were apparent once the breakthrough happened, resulting from the production of aqueous and oleic phases at the same time [24]. Within these fluctuations, the overall pressure drop shows a slight increment, reaching 1500 ± 10 mbar, after which it gradually decreased until it reached a steady-state pressure drop of 1300 ± 10 mbar. Subsequently, the flow rate was incrementally raised to 1 cm^3/min and later to 1.5 cm^3/min until the pressure drop stabilized. The primary reasons for implementing these higher flow rates were twofold: (a) to ensure that no further oil production could occur due to polymer flooding and (b) to estimate the end-point relative permeability for polymer flooding. Surprisingly, the observed pressure drops exceeded expectations for the SAV 10XV polymer, considering its viscosity and the anticipated reduction in permeability. This higher pressure drop was attributed to the formation of an emulsion, resulting in a substantial reduction in permeability. Consequently, the measured polymer end-point relative permeability was determined to be 0.03 ± 0.01, which is significantly lower than the water end-point relative permeability of 0.14 ± 0.01 as reported by Janssen et al. [22].

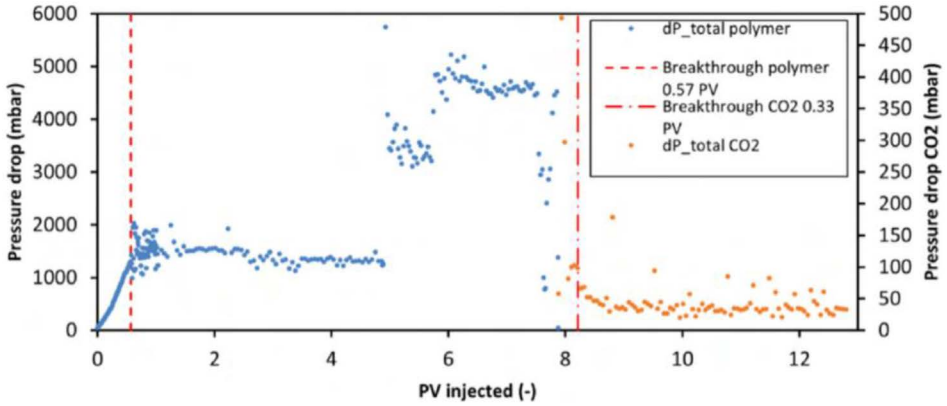

Figure 4—Pressure drop during both polymer flooding and CO_2 flooding for Exp. 1. Breakthrough of the polymer and CO_2 is achieved at 0.57 ± 0.03 PV and 0.33 ± 0.03 PV, respectively.

Following the completion of polymer flooding, CO_2 flooding was introduced. The breakthrough of CO_2 was observed at approximately 0.33 ± 0.03 PV injected, resulting in a rapid reduction in pressure drop. Subsequently, fluctuations in pressure were observed due to the production of various fluid phases at the outlet. Eventually, the pressure drop reached a steady state value of around 32 ± 3 mbar. Notably, as the system's backpressure was released, the CO_2 became visibly separated from the solution. Throughout the CO_2 flooding phase, the presence of a light emulsion persisted in the recovered fluids.

CT images. The displacement of oil by the polymer is depicted in Fig. 5. During polymer flooding, there is a displacement of oil (red/orange) by water (yellow/green) in a manner resembling a front, although with a less pronounced transition between regions of high and low water saturation. The S_o profiles during polymer flooding exhibit a behavior similar to that observed during primary drainage. Nonetheless, the region of the shock front appears to be less well-defined as a result of capillary forces exerting their influence. When end-point mobility ratios are less than 1, the displacement of oil by polymer exhibits a piston-like behavior. The averaged remaining oil saturation (S_{oR}) at the end of polymer flooding (0.31 ± 0.03) aligns closely with material balance calculations.

During the CO_2 injection, a clear gravity segregation is observed. The CO_2 predominantly bypasses the polymer, resulting in an early breakthrough at 0.33 ± 0.03 PV due to the contrasting density and viscosity between CO_2 and the polymer. Over the course of 5.67 ± 0.03 PV, the remaining oil saturation of 0.27 ± 0.03 is achieved which is only slightly lower than S_{oR} observed at the end of polymer flooding. The CT images reveal that parts of the core's bottom remain unswept by CO_2. It is worth mentioning that analysis of the CT images during CO_2 flooding shows a slight increase of 1–2 % in oil saturation, while oil is being recovered. This can be attributed to the oil swelling due to CO_2 dissolution into the oil phase. It is important to note that CO_2 dissolution into the oil and aqueous phases occurs in all other experiments as well; however, it is not clearly visible in the S_o profile due to higher saturation and recovery levels in those cases.

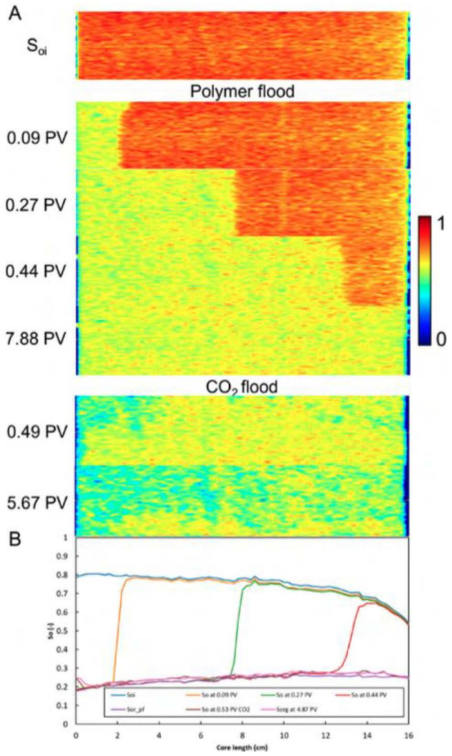

Figure 5—(A) The CT images taken during Exp. 1 with the from primary drainage on top, followed by polymer flooding as a secondary recovery mode and CO_2 flooding as a tertiary. (B) S_o profile across the core during the scans presented in A.

Oil recovery. Fig. 6 illustrates the recovery factor of Exp. 1, showcasing the percentage of total recovery achieved. The experiment resulted in a total recovery of 63.9 ± 3.1%. The majority of the recovery, 58.6 ± 3.1%, took place during polymer flooding, while only 5.3 ± 3.1% occurred during CO_2 flooding. During polymer flooding, a significant portion of the oil was recovered prior to the breakthrough of the polymer. After the breakthrough, only a minimal amount of oil was produced, as indicated by the water and oil cuts. The water cut is mostly 1, indicating the dominance of water production, while the oil cut is mostly 0, indicating minimal oil production. In contrast, during CO_2 flooding, all the recovery took place after the breakthrough. The phase cuts during CO_2 injection suggest that, after the breakthrough, the majority of the fluids produced at the outlet are composed of CO_2 itself.

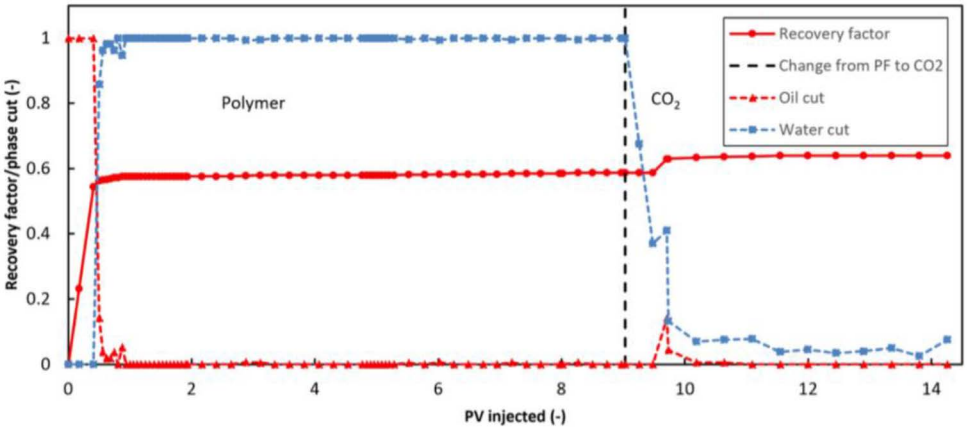

Figure 6—Oil cut, water cut, and oil recovery profiles for Exp. 1.

CO_2 flooding followed by polymer flooding (Exp. 2)

Pressure drop. Fig. 7 displays the pressure drop profile for Exp. 2, where CO_2 was used as a secondary recovery mode and polymer as a tertiary recovery mode. The profile exhibits a decreasing trend from the beginning of the CO_2 injection, primarily due to the rapid breakthrough of CO_2 through the initial sections of the core. The pressure drop decreased from the initial capillary entry pressure of 37 ± 3 mbar to 26 ± 3 mbar at the breakthrough point, which occurred at 0.42 ± 0.03 PV. Following the CO_2 breakthrough, the pressure drop sharply declined and demonstrates distinct fluctuations associated with the co-production of different fluid phases. The overall decreasing trend after breakthrough eventually reaches a steady-state pressure of 10 ± 3 mbar.

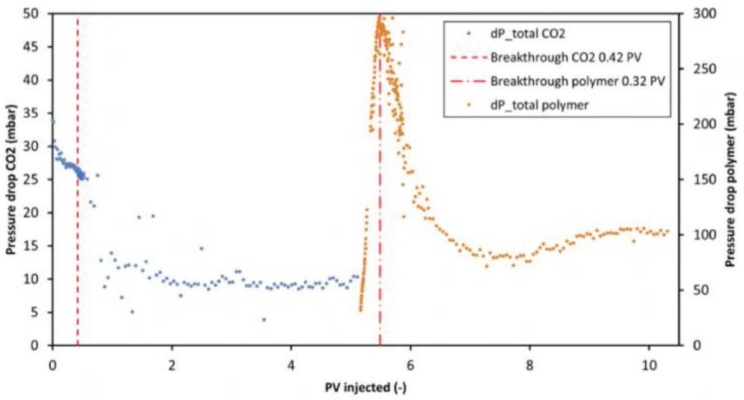

Figure 7—Total pressure drop profile during Exp. 2 (CO_2 flooding followed by polymer flooding). Breakthrough of CO_2 occurred at 0.42 PV. After nearly 5 PV of CO_2 injection, the polymer flood is initiated. The breakthrough of the polymer was reached at 0.32 ± 0.03 PV.

Upon switching to polymer flooding, there was a notable increase in the pressure drop, peaking at 292 ± 3 mbar at the breakthrough of the polymer at 0.32 ± 0.03 PV. Subsequently, the pressure drop rapidly decreased. This decline continued until it reaches the lowest point at 80 ± 3 mbar around 7.2 ± 0.03 cumulative PV injected. Afterward, the pressure drop starts to slightly increase again, reaching a steady-state value of 100 ± 3 mbar at the end of the polymer injection. The sharp decrease in pressure drop results from the swift breakthrough of the polymer through the CO_2-saturated top section of the core, leaving certain regions relatively unswept by the polymer at this stage. The subsequent increase in steady-state pressure indicates that the polymer has more uniformly filled the entire core. It is noteworthy that the maximum pressure drop observed during polymer flooding in Exp. 2 is considerably smaller compared to the pressure drop observed in Exp. 1 at a similar flow rate. This difference can be attributed to the absence of emulsion formation in Exp. 2.

CT images. Fig. 8 presents the CT images and corresponding S_o profiles for CO_2 and polymer flooding. Upon the introduction of gas into the core, the oil was promptly displaced and extracted through the outlet. During CO_2 injection, gravity segregation is evident as the much less dense CO_2 displaces the oil in the upper portion of the core. This results in a rapid breakthrough of CO_2 at 0.42 ± 0.03 PV. Moreover, the displacement dynamics observed during CO_2 flooding were influenced by sub-core scale heterogeneity. Despite Bentheimer being recognized as a relatively homogeneous sandstone, our CT analysis revealed a slight deviation of approximately 0.3% in the porosity values along the length of the core. This finding suggests the presence of micro-scale heterogeneity within the rock formation. The CO_2 front propagation primarily occurred within the higher-porosity parts of the core. Subsequently, CO_2 migrated into other regions with lower porosity. This resulted in the bypassing of smaller pores and low-permeability regions in both high- and low-porosity layers, leading to relatively elevated levels of irreducible water saturation.

Following the initial breakthrough at the front, CO_2 begins to fill other parts of the core, leading to an increase in measured CO_2 saturation in each identified region of interest. Consequently, oil production persisted throughout approximately 5 PV of CO_2 injection, predominantly from the upper section of the core before breakthrough and primarily from the lower section after breakthrough. Nevertheless, substantial portions of the bottom section remained unswept, resulting in a relatively high value of S_{oR} (0.43 ± 0.03).

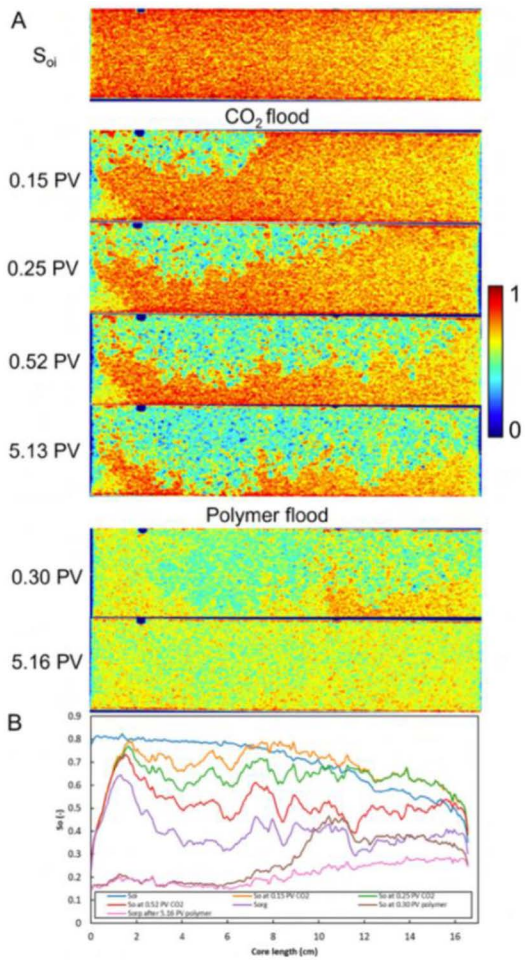

Figure 8—(A) CT images taken during the injection of the different fluid phases from which S_o is determined. The scan is presented on top, followed by CO_2 flooding and polymer flooding images. (B) S_o profile during the whole of the secondary and tertiary injection modes.

Following CO_2 flooding, polymer flooding was initiated. Just before the breakthrough of the polymer at 0.32 ± 0.03 PV, the polymer is observed to sweep some of the oil across the core, although some parts remain unswept, particularly in the bottom section. This sweeping of the polymer is reflected in a significant decrease in S_o in the first half of the core. Throughout the complete injection of the polymer phase, the core exhibits relatively even sweeping, resulting in an S_{oR} of 0.19 ± 0.03. It is important to note, similar to Exp. 1, the majority of oil recovery took place prior to the breakthrough of the polymer.

Oil recovery. The recovery and fluid cut data for Exp. 2 are depicted in Fig. 9. Prior to the breakthrough of CO_2, approximately 26 ± 3% of the original oil in place (OIIP) was recovered, accounting for 68% of the total oil recovery achieved through CO_2 injection. Following the injection of approximately 5 PV of CO_2, the total recovery factor reached 38.8 ± 3.0%. Subsequently, polymer flooding was implemented as the tertiary recovery method. A significant incremental recovery of 33.6 ± 3.0% was observed, with the majority of the recovery occurring before the breakthrough of the polymer phase. Overall, a total recovery

of 72.4 ± 3.2% was achieved through polymer flooding after CO_2 injection. The substantial incremental recovery by the polymer can be attributed to two main factors. Firstly, the unswept portion of the core left by CO_2 allowed for further recovery by the polymer, which is less susceptible to gravity segregation due to its smaller density contrast with the oil phase. Secondly, the injection of CO_2 under immiscible conditions results in the dissolution of CO_2 into both the polymer solution and the remaining oil present in the core. As a result of CO_2 dissolution in oil, the viscosity of the oil is decreased, resulting in a more favorable mobility ratio between the high-viscosity polymer and the now less viscous oil.

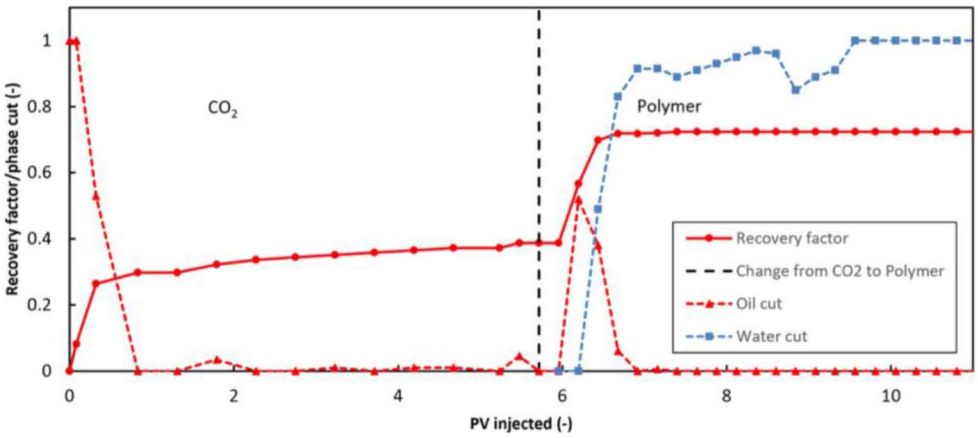

Figure 9—Oil cut, water cut, and oil recovery profiles for Exp. 2.

WAG vs. PA-WAG

In this section, we present a comparative analysis of the results obtained from the WAG (Water Alternating Gas, Exp. 3) core-flood experiment and the PA-WAG (Polymer-Assisted Water Alternating Gas, Exp. 4) core-flood experiment. The purpose is to emphasize the variations and distinctions between these two injection schemes.

Pressure drop. Fig. 10 displays the total pressure drop profile for both WAG and PA-WAG injection schemes. The injection cycles commenced with the introduction of an aqueous phase slug, either brine for WAG or polymer for PA-WAG, at a flow rate of 2 cm^3/min, followed by a CO_2 slug injection at 0.5 cm^3/min. Both experiments exhibit similar pressure drop profiles due to their comparable injection schemes. The pressure drop trend during the polymer slug injection in the first cycle of PA-WAG is comparable to the pressure drop observed in Exp 1. The viscosity difference between the phases in the PA-WAG experiment results in a higher pressure drop during the injection of polymer slugs compared to brine slugs in the WAG injection. During the first cycle, when the shift to CO_2 occurs, the pressure drop decreases from 127 ± 3 to 50 ± 5 mbar in the WAG injection, and from 841 ± 5 to 80 ± 5 mbar in the PA-WAG injection.

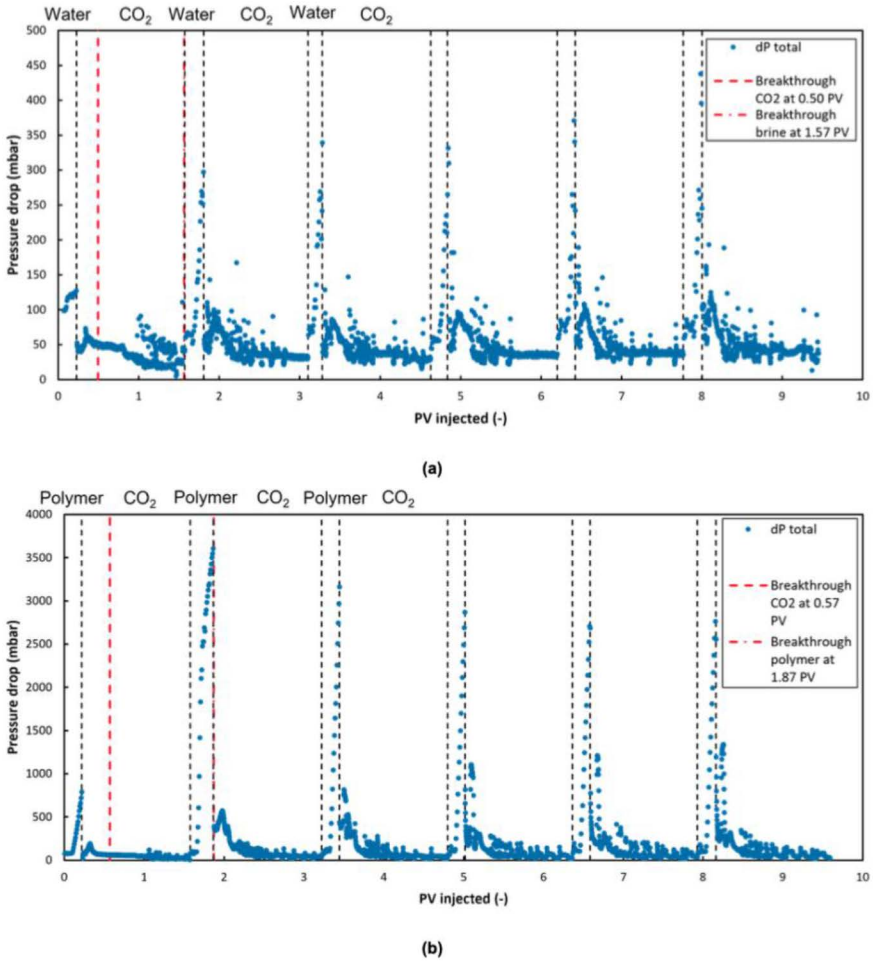

Figure 10—Pressure drop profiles during (a) WAG injection (Exp. 3) and (b) PA-WAG injection (Exp. 4).

For the second CO_2 slug, the overall steady trend of the pressure drop was slightly increased, most probably due to the presence of trapped gas saturation as reported by Janssen et al. [20] and enlarged S_w, from 25 ± 3 to 35 ± 5 mbar for the WAG injection and 30 ± 5 to 45 ± 5 mbar for the PA-WAG injection. This steady-state pressure drop remained for the following cycles approximately the same for the gas slug.

The breakthrough of the aqueous phase and CO_2 were determined using the combination of CT images and pressure data. The brine and polymer breakthroughs are found at 0.22 and 0.51 PV in terms of the aqueous phase injected (0.22 and 1.87 PV of cumulative injection), having a significant delay of aqueous phase breakthrough between WAG and PA-WAG injections by a whole injection slug due the addition of polymer. The breakthrough of CO_2 was observed at 0.27 ± 0.03 PV and 0.35 ± 0.03 PV of injected CO_2 (0.50 ± 0.03 PV and 0.57 ± 0.03 PV of cumulative injection) for the WAG and PA-WAG experiments, respectively. These findings indicate that the polymer used in the PA-WAG injection slightly delayed the breakthrough of CO_2 compared to the WAG injection, despite using cores with similar properties.

CT images. Fig. 11 and 12 provide the saturation profiles and corresponding CT images obtained during the injection of both WAG and PA-WAG. These profiles demonstrate a highly similar saturation pattern throughout the CT scans. In the CT scans, the oleic phase is visualized as a blue/green color, the aqueous phase as light blue/white, and CO_2 as white. It is worth noting that the cores employed in both the WAG and PA-WAG experiments possessed comparable permeability and initial oil saturation, enabling a meaningful comparison of displacement mechanisms between the two experiments.

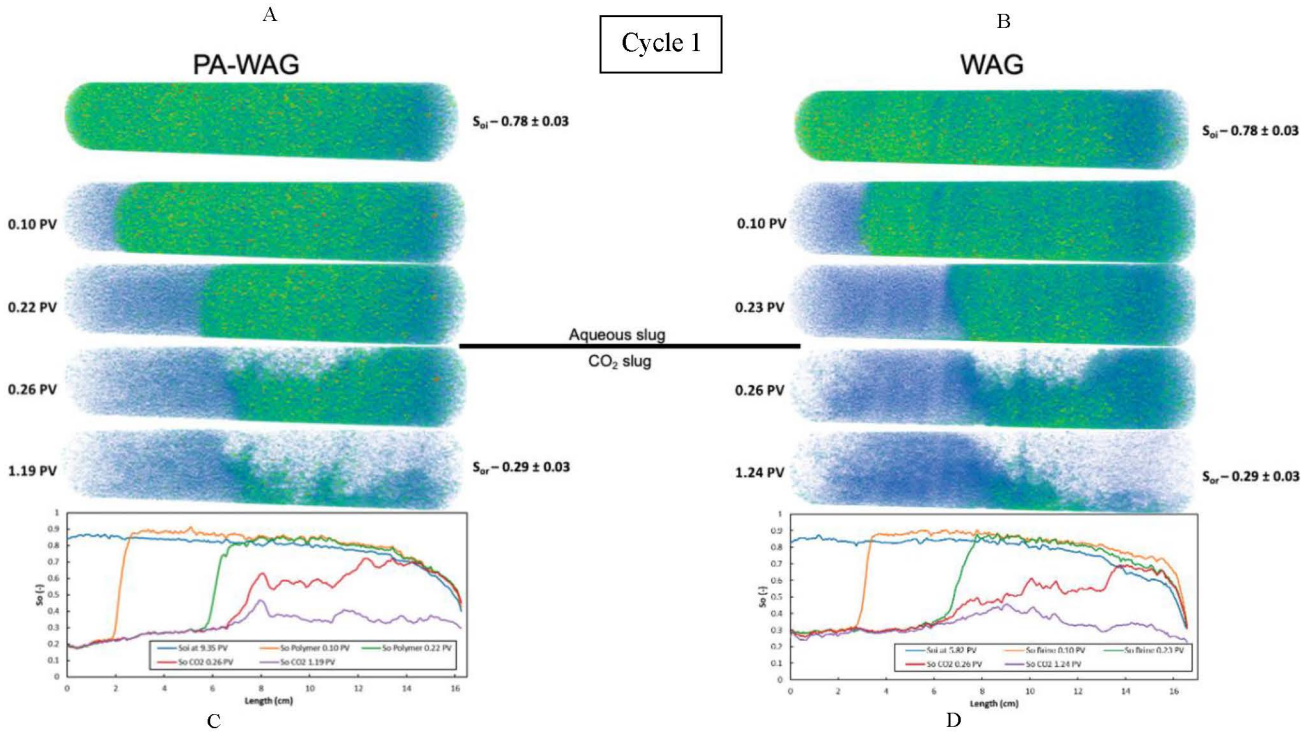

Figure 11—CT images taken and oil saturation profiles during the first cycle of PA-WAG and WAG injection. (A) CT images during PA-WAG injection and (B) CT images during WAG injection. Oil saturation profiles during (C) PA-WAG injection and (D) WAG injection.

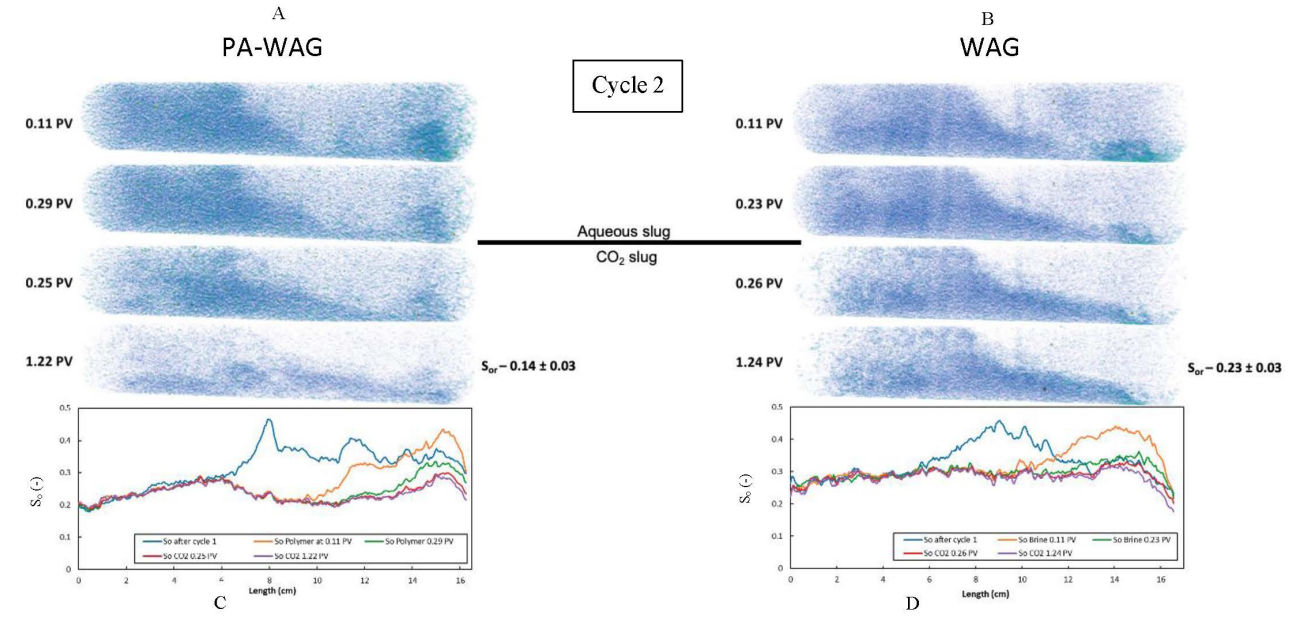

Figure 12—CT images taken and oil saturation profiles during the second cycle of PA-WAG and WAG injection. (A) CT images during PA-WAG injection and (B) CT images WAG injection during. Oil saturation profiles during (C) PA-WAG injection and (D) WAG injection.

As discussed in the primary drainage section, the accumulation of the aqueous phase at the end of the oil injection is observed in both the WAG and PA-WAG cases. During the injection of the brine and polymer slug in the first cycle, the displacement front remains stable, effectively sweeping the beginning of the core. However, it appears that the polymer front moves more slowly as compared to the water front. The stability of the front is influenced by the balance of various forces such as gravity, capillary, viscous forces, and dispersion acting on the interface. Due to the relatively lower viscosity of oil, even during water

flooding, the front appears to be relatively stable. When the viscosity of the driving water is increased, due to water-soluble polymers, the mobility ratio (M) decreases to values below 1 ($M < 1$). This reduction in the fractional flow of water causes a shift in the fractional flow curve towards the right. Consequently, the average saturation of water increases. This leads to a more effective displacement of the oil, resembling a piston-like movement, resulting in a higher displacement of oil and a delay in the advancement of the aqueous phase front. At the end of the brine slug injection (0.23 ± 0.03 PV), a slight segregation is observed in the front. This segregation is attributed to the higher mobility ratio between the oil and brine compared to the mobility ratio between oil and polymer. As a result, the bottom section of the displacement front appears slightly ahead of the top section. On the other hand, this segregation is not evident in the first polymer slug at 0.22 ± 0.03 PV. Notably, the presence of an oil bank can be observed in front of both the brine and polymer throughout the entire first cycle, as indicated by the retrieved S_o.

Upon the injection of CO_2 in the first cycle, clear segregation occurs for both WAG and PA-WAG due to the significantly lower density of CO_2 compared to the existing phases in the core. The CO_2 bypasses a large portion of the brine and polymer present in the first half of the core, displacing the oil primarily at the top section beyond the displacement front created by the aqueous slugs. In the WAG experiment, the CO_2 slug visibly accumulates at the inlet of the core, whereas in the PA-WAG experiment, the CO_2 is more evenly distributed throughout the polymer-occupied section of the core. At approximately 0.26 ± 0.03 PV (from the start of CO_2 injection) for both WAG and PA-WAG, the CO_2 forms a small oil bank near the end of the core before the saturation (S_o) experiences a sharp decline due to the capillary end effect. A notable observation from the CT scans is that during the injection of the first CO_2 slug, the polymer front remained stationary at the position it reached during the polymer slug injection at the end of polymer injection for cycle 1. In contrast, the water front during WAG injection did not remain stationary and infiltrated the last section of the core. This difference in behavior resulted in the early breakthrough of water at the end of the first cycle, while the polymer front remained stationary during CO_2 injection, causing a delay in breakthrough until the end of the second polymer slug injection. At the conclusion of the first cycle (Fig. 11), a notable portion of the bottom section of the core remains relatively unswept by both brine or polymer and CO_2 in both the WAG and PA-WAG experiments. The first cycles in both experiments result in an S_{oR} of 0.29 ± 0.03.

In the second cycle of both WAG and PA-WAG injections (Fig. 12), a significant impact can be observed in terms of oil displacement from the center bottom part of the core, which was left behind during the first cycle. In both the CT images and the saturation profiles (S_o), it is evident that this oil is displaced, forming an oil bank towards the end of the core at approximately 0.11 ± 0.03 PV in both experiments. At the end of the aqueous phase injection in both experiments, some accumulation of oil is still present at the end of the core, primarily in the bottom section.

Upon switching to CO_2 injection in the second cycle, the S_o remains unchanged in the first half of the core throughout the entire slug injection. However, there is an overall change in saturation throughout the core, as the CT images represent multiple phases. In the PA-WAG experiment, the degree of gravity segregation observed for CO_2 is less severe compared to the WAG experiment and CO_2 appears to be more evenly spread out over the core. In the WAG experiment, on the other hand, CO_2 accumulates more at the top and end sections. Due to the reduced gravity segregation in the PA-WAG experiment, the oil bank formed at the bottom end of the core during the aqueous phase injection is effectively recovered. In contrast, a considerable portion of the bottom end section of the core remains unswept in the WAG experiment. As a result, there is a notable disparity in the oil recovery, with an S_{oR} of 0.23 ± 0.03 for WAG and 0.14 ± 0.03 for PA-WAG at the end of the second cycle.

Only small decreases in S_o are observed over the remaining four cycles of injection for both WAG and PA-WAG, mainly at the core's beginning and end sections. The overall fluid saturation displayed in the CT images decreases in both experiments, with the most noticeable change occurring in the bottom center

section of the core. Upon completion of the full WAG and PA-WAG injections, the achieved S_{oR} for the experiments is 0.19 ± 0.03 and 0.11 ± 0.03, respectively.

Oil recovery. Fig. 13a and 13b illustrate the development of recovery factors and the corresponding oil and water cuts for both the WAG (Exp. 3) and PA-WAG (Exp. 4) experiments. During the first cycle, the oil recovered is highly similar between the two experiments, with a recovery factor of 62 ± 3% for both cases. This accounts for approximately 81% and 73% of the total recovery for WAG and PA-WAG, respectively. The majority of this recovery occurs after the breakthrough of CO_2 in both experiments. The key difference in terms of sweep efficiency and recovery between WAG and PA-WAG injections is observed during the second cycle. For WAG, the recovery factor increases to 71 ± 3%, while PA-WAG achieves a higher recovery factor of 82 ± 3%. This leads to 94% and 96% of the total recovery being achieved for WAG and PA-WAG, respectively. In both experiments, the bulk of this recovery takes place with the breakthrough of the aqueous phase. For WAG, this occurs at the start of the second brine slug injection, while for PA-WAG, it happens at the end of the second polymer slug injection. During the remaining four cycles, only minimal amounts of oil are recovered. Notably, the production of oil coincides with the production of the aqueous phase for cycles 2 to 6 in both WAG and PA-WAG. However, in PA-WAG, emulsions are recovered from the production of polymer starting from the fourth cycle until the end of production. The complete WAG and PA-WAG recovery injection schemes resulted in total recovery factors of 76 ± 3% and 86 ± 3%, respectively.

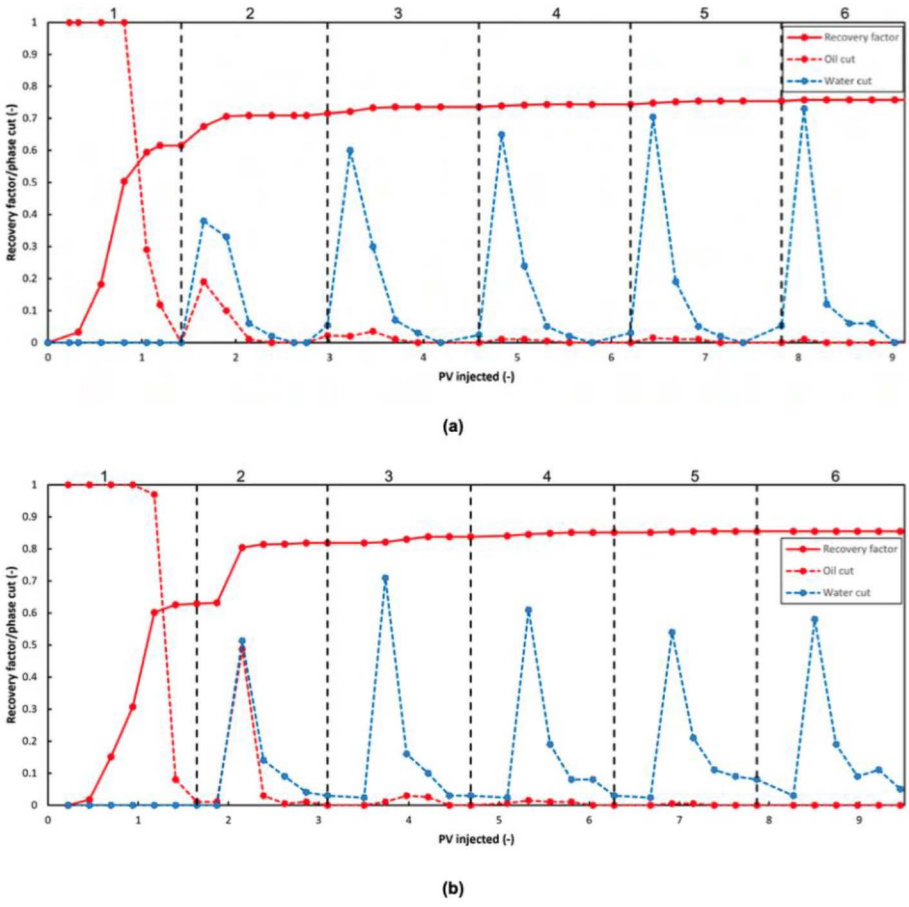

Figure 13—Oil cut, water cut, and oil recovery profiles for (a) Exp. 3 and (b) Exp. 4. The numbers on top of the graph show the cycle number.

General discussion

In this section, we revisit the findings of our study and analyze them within the framework of a conceptual model that explains the factors contributing to the improvement in oil recovery during PA-WAG injection.

Fig. 14 provides a comprehensive overview of the recovery factors achieved during the different stages of injection in the four core-flood experiments. The results highlight the advantages of PA-WAG over WAG injection, as well as CO_2 and polymer flooding, specifically in Bentheimer sandstone cores.

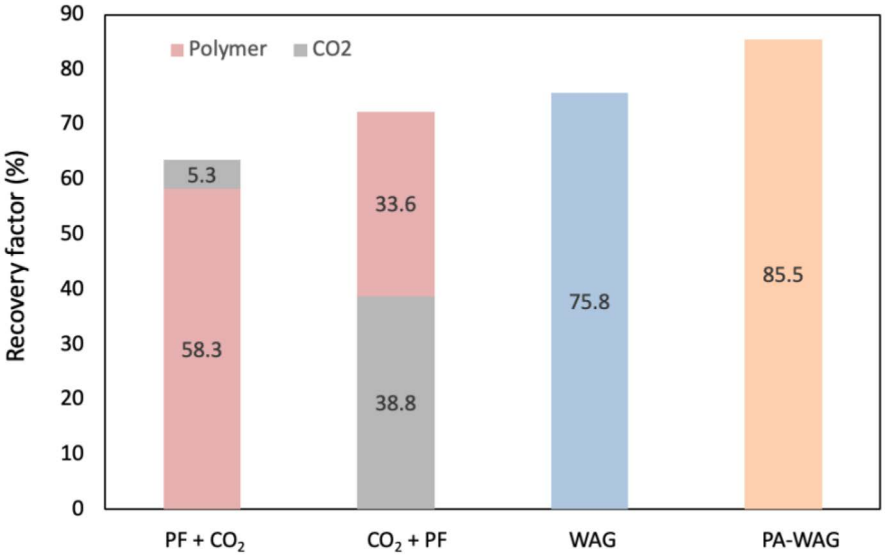

Figure 14—Comparison of the recovery factors of the four core-flood experiments carried out in this study.

In the secondary injection modes, polymer flooding resulted in an *RF* of 58.3 ± 0.5% of OOIP, while CO_2 flooding achieved a lower *RF* of 38.8 ± 0.8%. Introducing CO_2 as a tertiary injection mode after polymer flooding (Exp. 1) had only a marginal impact, with an incremental *RF* of 5.3 ± 0.8%. However, when the polymer was injected as a tertiary mode after polymer flooding (Exp. 2), a significant improvement in recovery was observed, with an incremental *RF* of 33.6 ± 0.8%. The in-situ visualization of CO_2 displacement revealed notable gravity segregation due to the contrasting densities of CO_2 and oil. This explains the relatively low *RF* observed during continuous CO_2 injection.

The injection of WAG nearly doubled the oil recovery, achieving an *RF* of 76.0 ± 0.5% compared to continuous CO_2 injection. However, water and gas breakthrough still occurred early in the injection process, with water breakthrough at 0.22 PV and CO_2 breakthrough at 0.27 PV. The addition of polymer to the aqueous phase in the PA-WAG injection delayed both water and CO_2 breakthroughs, which occurred at 0.51 PV for water and 0.35 PV for CO_2. Moreover, PA-WAG exhibited less severe gravity segregation of CO_2 compared to WAG injection. This resulted in an additional ~10% increase in the recovery factor. Overall, the results demonstrate the favorable effects of PA-WAG over WAG injection and the limited impact of continuous CO_2 injection, highlighting the potential of PA-WAG as an effective oil recovery method in Bentheimer sandstone cores.

The primary hypothesis for the improved recovery observed in PA-WAG compared to WAG injection is based on two factors: the delay in water breakthrough and the delay in CO_2 breakthrough.

The delay in water breakthrough can be attributed to the higher viscosity of water, which is achieved by the presence of water-soluble polymers. The increased viscosity of the aqueous phase leads to a more stable displacement front, allowing for better sweep efficiency and improved displacement of the oil phase. The delayed water breakthrough ensures that more oil is displaced and recovered before the water phase reaches the production well.

Our hypothesis regarding the delay in CO_2 breakthrough during PA-WAG injection is supported by (a) the mechanisms of gravity override reduction and (b) micro-scale heterogeneity reduction through polymer adsorption.

Considering the driving forces of gravity and viscosity in CO_2 displacement, when gravity is dominant, gravity segregation occurs more rapidly than horizontal displacement [25]. However, by increasing the viscosity of water through the addition of water-soluble polymers, the contribution of viscous forces to the total flux increases. This leads to a decrease in the dominance of gravity and a more balanced contribution between gravity and viscosity. Consequently, CO_2 becomes slightly more inclined to move in the horizontal direction, resulting in a less severe gravity override. This hypothesis explains the observed delay in CO_2 breakthrough during PA-WAG injection.

Furthermore, the presence of polymer adsorption onto the rock surface during polymer injection plays a role in reducing micro-scale heterogeneity. The adsorbed polymer molecules create barriers and modify the permeability distribution within the reservoir. This reduction in permeability variations helps mitigate gas channeling and uneven flow paths, promoting a more controlled and uniform displacement of CO_2. The delayed CO_2 breakthrough observed during PA-WAG injection aligns with the hypothesis of reduced micro-scale heterogeneity.

The quantification of polymer adsorption, with an average of 79.0 ± 0.5 μg polymer/g rock, further supports the notion of reduced heterogeneity. The resulting residual resistance factor of 1.8 which led to a permeability reduction by 35% indicates increased flow resistance and a more uniform flow profile, contributing to the delay in CO_2 breakthrough.

Overall, the combined effects of reducing gravity override and micro-scale heterogeneity through polymer adsorption provide a plausible explanation for the observed delay in CO_2 breakthrough during PA-WAG injection as clearly demonstrated through in-situ visualization. This confirms the effectiveness of the PA-WAG injection method in delaying the gas breakthrough which has been a major issue for WAG injection in field applications.

Conclusions

This experimental study presents valuable insights into the performance and displacement mechanisms of Polymer Assisted-Water-Alternating-Gas (PA-WAG) injection and compares it with other oil recovery methods. The key conclusions drawn from this study are as follows:

- Polymer injection alone achieved a recovery factor of approximately 59% in the secondary recovery phase, outperforming the CO_2 injection alone which only resulted in a recovery factor of around 38%.
- Introducing polymer in the tertiary mode led to an additional recovery factor of about 34%, whereas CO_2 injection in the tertiary mode only resulted in a marginal incremental recovery of approximately 5%.
- The analysis of CT data revealed a piston-like displacement of oil by polymer, indicating its effective sweep efficiency. In contrast, strong gravity segregation of CO_2 was observed during the displacement process.
- The inclusion of a polymer in the water slug, forming the PA-WAG injection method, resulted in an additional recovery of approximately 10% compared to traditional WAG injection.
- PA-WAG injection exhibited improved sweep efficiency by mitigating the issue of CO_2 gravity segregation. Consequently, CO_2 breakthrough was delayed during PA-WAG injection compared to WAG injection.
- These findings highlight the potential of PA-WAG as an effective oil recovery method, offering higher recovery factors and improved sweep efficiency compared to conventional injection approaches.

Acknowledgments

This research forms part of the research program of DPI, project #849. The work of [Thijs van Wieren, Ali Fadili, Diederik van Batenburg, Thierry Leblanc, and Pacelli Zitha] forms part of the research program of DPI, project #849' is included. The authors thank Michiel Slob, and Ellen Meijvogel-de Koening for technical support. Ronald Korstanje is acknowledged for fruitful discussions.

References

1. Wang, Y.; Vuik, C.; Hajibeygi, H. CO2 Storage in deep saline aquifers: impacts of fractures on hydrodynamic trapping. *International Journal of Greenhouse Gas Control* 2022, **113**, 103552, doi: https://doi.org/10.1016/j.ijggc.2021.103552.
2. Celia, M.A.; Bachu, S.; Nordbotten, J.M.; Bandilla, K.W. Status of CO2 storage in deep saline aquifers with emphasis on modeling approaches and practical simulations. *Water Resources Research* 2015, **51**, 6846–6892, doi: https://doi.org/10.1002/2015WR017609.
3. Kalyanaraman, N.; Arnold, C.; Gupta, A.; Tsau, J.S.; Ghahfarokhi, R.B. Stability improvement of CO2 foam for enhanced oil-recovery applications using polyelectrolytes and polyelectrolyte complex nanoparticles. *Journal of Applied Polymer Science* 2017, 134, doi: https://doi.org/10.1002/app.44491.
4. Massarweh, O.; Abushaikha, A.S. A review of recent developments in CO2 mobility control in enhanced oil recovery. *Petroleum* 2022, **8**, 291317, doi: https://doi.org/10.1016/j.petlm.2021.05.002.
5. Carpenter, C. Gelled Emulsions of CO2, Water, and Nanoparticles. *Journal of Petroleum Technology* 2014, **66**, 135–137, doi: 10.2118/0714-0135-jpt.
6. Chakravarthy, D.; Muralidaharan, V.; Putra, E.; Hidayati, D.T.; Schechter, D.S. Mitigating Oil Bypassed in Fractured Cores During CO2 Flooding Using WAG and Polymer Gel Injections. In *Proceedings of the SPE/DOE Symposium on Improved Oil Recovery*, 2006.
7. Zitha, M.M.Y.E.B.P. Mechanistic Simulation and History Matching of Alkaline-Surfactant-Polymer ASP Core Flooding Experiment at Optimum vs. Under-Optimum Salinity Conditions. In *Proceedings of the SPE Europec featured at 81st EAGE Conference and Exhibition*, London, England, UK, 2019.
8. Rahimi, V.; Bidarigh, M.; Bahrami, P. Experimental Study and Performance Investigation of Miscible Water-Alternating-CO2 Flooding for Enhancing Oil Recovery in the Sarvak Formation. *Oil & Gas Science and Technology - Rev. IFP Energies nouvelles* 2017, **72**, 35.
9. Afzali, S.; Rezaei, N.; Zendehboudi, S. A comprehensive review on Enhanced Oil Recovery by Water Alternating Gas (WAG) injection. *Fuel* 2018, **227**, 218–246, doi: https://doi.org/10.1016/j.fuel.2018.04.015.
10. Christensen, J.R.; Stenby, E.H.; Skauge, A. Review of WAG Field Experience. *SPE Reservoir Evaluation & Engineering* 2001, **4**, 97–106, doi: 10.2118/71203-pa.
11. Liu, M.K.; Andrianov, A.I.; Rossen, W.R. Sweep Efficiency in CO2 Foam Simulations With Oil. In *Proceedings of the SPE EUROPEC/EAGE Annual Conference and Exhibition*, 2011.
12. Lien, S.C.; Lie, S.E.; Fjellbirkeland, H.; Larsen, S.V. Brage Field, Lessons Learned After 5 Years of Production. In *Proceedings of the European Petroleum Conference*, 1998.
13. Choi, J.; Jeong, M.S.; Park, K.; Lee, K.S. CO2 WAG Process with Gel Treatment Considering Flowing Gel Viscosity in Heavy Oil Reservoir. In *Proceedings of the The Twenty-fifth International Ocean and Polar Engineering Conference*, 2015.
14. Mirzaie Yegane, M.; Boukany, P.E.; Zitha, P. Fundamentals and Recent Progress in the Flow of Water-Soluble Polymers in Porous Media for Enhanced Oil Recovery. *Energies* 2022, **15**, 8575.

15. Zhang, Y.; Huang, S.S.; Luo, P. Coupling Immiscible CO2 Technology and Polymer Injection to Maximize EOR Performance for Heavy Oils. *Journal of Canadian Petroleum Technology* 2010, **49**, 25–33, doi: 10.2118/137048-pa.
16. Li, W.; Schechter, D.S. Using Polymer Alternating Gas to Maximize CO2 Flooding Performance. In *Proceedings of the SPE Energy Resources Conference*, 2014.
17. Tovar, F.D.; Barrufet, M.A.; Schechter, D.S. Experimental Investigation of Polymer Assisted WAG for Mobility Control in the Highly Heterogeneous North Burbank Unit in Oklahoma, Using Anthropogenic CO2. In *Proceedings of the SPE Latin American and Caribbean Petroleum Engineering Conference*, 2015.
18. Kong, X.; Delshad, M.; Wheeler, M.F. A Numerical Study of Benefits of Adding Polymer to WAG Processes for a Pilot Case. In *Proceedings of the SPE Reservoir Simulation Symposium*, 2015.
19. Yang, Y.; Li, W.; Zhou, T.; Dong, Z. Using Polymer Alternating Gas to Enhance Oil Recovery in Heavy Oil. *IOP Conference Series: Earth and Environmental Science* 2018, **113**, 012182, doi: 10.1088/1755-1315/113/1/012182.
20. Abbas, A.H.; Abdullah, D.S.; Jaafar, M.Z.; Wan Sulaiman, W.R.; Agi, A. Comparative numerical study for polymer alternating gas (PAG) flooding in high permeability condition. *SN Applied Sciences* 2020, **2**, 938, doi: 10.1007/s42452-020-2673-8.
21. Peksa, A.E.; Wolf, K.-H.A.A.; Zitha, P.L.J. Bentheimer sandstone revisited for experimental purposes. *Marine and Petroleum Geology* 2015, **67**, 701–719, doi: https://doi.org/10.1016/j.marpetgeo.2015.06.001.
22. Janssen, M.T.G.; Pilus, R.M.; Zitha, P.L.J. A Comparative Study of Gas Flooding and Foam-Assisted Chemical Flooding in Bentheimer Sandstones. *Transport in Porous Media* 2020, **131**, 101–134, doi: 10.1007/s11242-018-01225-3.
23. Huang, D.D.; Honarpour, M.M. Capillary end effects in coreflood calculations. *Journal of Petroleum Science and Engineering* 1998, **19**, 103117, doi: https://doi.org/10.1016/S0920-4105(97)00040-5.
24. Mirzaie Yegane, M.; Schmidt, J.; Dugonjic-Bilic, F.; Gerlach, B.; Boukany, P.E.; Zitha, P.L.J. Flow Enhancement of Water-Soluble Polymers through Porous Media by Preshearing. *Industrial & Engineering Chemistry Research* 2021, **60**, 3463–3473, doi: 10.1021/acs.iecr.1c00099.
25. Moyner, O.; Nilsen, H.M. Multiresolution coupled vertical equilibrium model for fast flexible simulation of CO2 storage. *Computational Geosciences* 2019, **23**, 1–20, doi: 10.1007/s10596-018-9775-z.